Numerical Heat Transfer, Part A, 49: 215–236, 2006

ISSN: 1040-7782 print/1521-0634 online
DOI: 10.1080/10407780500324996

Taylor & Francis
Taylor & Francis Group

NUMERICAL SIMULATION OF LASER-PRODUCED PLASMA DEVICES FOR EUV LITHOGRAPHY USING THE HEIGHTS INTEGRATED MODEL

V. Sizyuk, A. Hassanein, V. Morozov, V. Tolkach, and T. Sizyuk
Energy Technology Division, Argonne National Laboratory, Argonne, Illinois, USA

B. Rice
Component Research Division, Intel Corporation, Hillsboro, Oregon, USA

Laser-produced plasma (LPP) devices have been modeled as the light source for extreme ultraviolet (EUV) lithography. A key challenge for LPP is achieving sufficient brightness to support the throughput requirements of high-volume manufacturing. An integrated model (HEIGHTS) was applied to simulate the environment of EUV sources and optimize their output. The model includes plasma evolution and magnetohydrodynamic processes in a two-temperature approximation, as well as photon radiation transport determined by the Monte Carlo method. It uses the total variation diminishing scheme for the description of magnetic compression and diffusion in a cylindrical 2-D geometry for the target. Generation of the internal magnetic field with nonparallel density and temperature gradients was also considered. Preliminary results from numerical simulation in hydrodynamics and line radiation output of xenon and tin plasmas are presented for planar and droplet targets.

INTRODUCTION

The extreme ultraviolet (EUV) lithography community has made several important contributions to improving the radiation source device. Recent advances in laser systems with a high repetition rate and high average power suggest the feasibility of modular, flexible, and relatively inexpensive microelectronic production facilities based on laser plasma sources. Challenges remain. Modern projection lithography systems require [1, 2] as a minimum 1% conversion efficiency of laser light into soft X-rays within a 2% bandwidth at 13.5 nm, where multilayer reflectivity of more than 60% can be routinely achieved by Mo-Si mirrors. Final in-band power must be obtained, with an intermediate focus over 115 W. These requirements

Received 27 April 2005; accepted 15 July 2005.
The authors wish to acknowledge the support of the Intel Corporation for a major portion of this work.
Argonne National Laboratory is operated by the University of Chicago for the U.S. Department of Energy under Contract W-21-109-Eng-38.
Address correspondence to A. Hassanein, Argonne National Laboratory, 9700 S. Cass Ave., Bld. 308, Argonne, IL 60439-4825, USA. E-mail: hassanein@anl.gov

NOMENCLATURE

A, C, D	linear coefficients
$\mathbf{B}$	magnetic field
c	light speed
c_p	specific heat
e	electron charge
e_e	electron specific internal energy
e_i	ion specific internal energy
$\mathbf{F, G, P}$	convective fluxes
K_{BS}	inverse bremsstrahlung coefficient
k_B	Boltzmann constant
$\ln \Lambda$	Coulomb logarithm
n	concentration
p	pressure
Q	external source
t	time
T	temperature
$\mathbf{U}$	vector of solution
v	plasma velocity
Z	ionic specific charge
Δr	step by r axis
Δt	time step
Δz	step by z axis
η	resistivity
λ	thermal conductivity
μ	magnetic permeability
ν	frequency of laser light
ν_p	plasma frequency
τ_e	time between electron interactions
Ω	cyclotron frequency
$\mathbf{\Omega}$	vector of external source

Subscripts

e	electrons
i	ions
m	magnetic
tot	total

Superscripts

n	time-step number
r	by r axis
z	by z axis

necessitate investigation and optimization not only of laser power sources but also laser irradiation parameters, laser energy deposition, target material, target design, etc. In addition, the multidimensional processes of plasma motion fill a very important place. Solving problems related to these requirements is best done by computer simulation and benchmarking with available experimental data.

For that purpose, an integrated magnetohydrodynamics (MHD) model and its base HEIGHTS code [3–5] are used to describe the hydrodynamics and optical processes that occur in laser-generated plasmas. The model considers four main processes: laser radiation absorption, plasma evolution by generation of a magnetic field, radiation transport, and EUV generation in the 13.5-nm diapason. The integrated model includes the total variation diminishing (TVD) scheme in the Lax-Friedrich formulation [6, 7] for the description of the laser-produced plasma motion, an implicit scheme with sparse matrix solver for heat transport and magnetic diffusion processes, and the weight Monte Carlo model [8, 9] for radiation transport and EUV output simulation. Several models [10–12] are being developed and can be used to calculate opacity: a collision radiation equilibrium (CRE) model, which is a self-consistent model that takes into account Auger processes, and a nonstationary kinetic model that depends on the complexity of the problem and the availability of computer time. Different sets of opacities for the MHD and the EUV calculations were used: (1) 3,693 spectral groups for Xe and 3,240 groups for Sn in a wide range, and (2) about 2,500 spectral points for Xe and up to 5,000 spectral points for Sn within the EUV region.

This article paper describes our initial simulation of MHD and optical processes that occur in laser-produced plasma (LPP) devices in which the target has a planar and droplet geometry. Xenon and tin were tested as target materials.

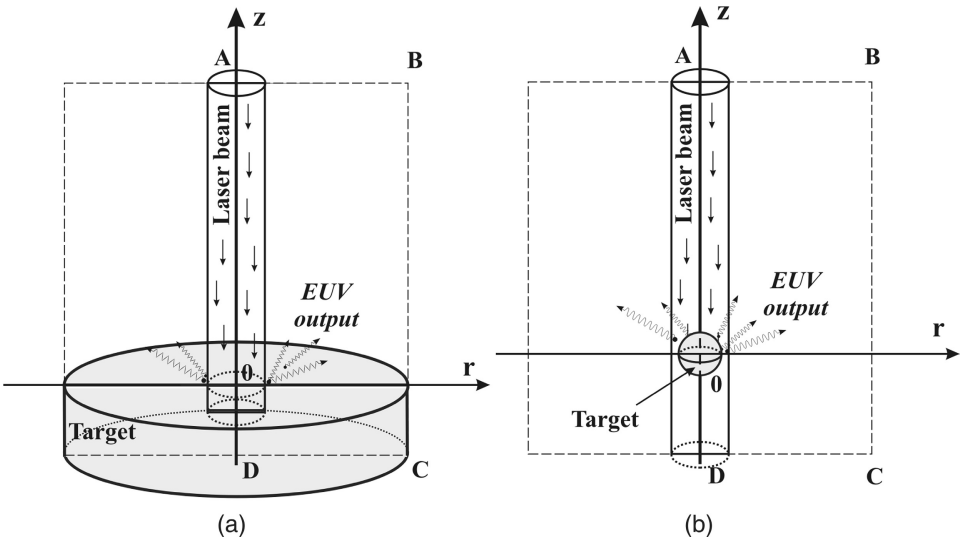

Figure 1. Schematic view of LPP device: (*a*) planar target; (*b*) droplet target.

Schematically simulated LPP devices in 2-D cylindrical geometry are shown in Figure 1. The device chamber is filled by the working gas under an initial pressure in the range of several tens of mbar at room temperature, corresponding to an initial density of the gas in the range of 10^{14}–$10^{15}\,\mathrm{cm}^{-3}$. It is also assumed that the target material is preheated to a temperature of $\sim$1eV.

MATHEMATICAL MODEL

We consider the general set of 3-D resistive MHD equations [6] expanded with heat transport fluxes, radiation fluxes, and a thermomagnetic source term. The general set is presented in two-temperature approximation. In Gaussian units, the full set is given by

$$\frac{\partial \rho}{\partial t} + \nabla \cdot (\rho \mathbf{v}) = 0 \tag{1}$$

$$\frac{\partial \rho \mathbf{v}}{\partial t} + \nabla \cdot \left(\rho \mathbf{v}\mathbf{v} + p_{\mathrm{tot}} - \frac{1}{4\pi\mu}\mathbf{B}\mathbf{B} \right) = 0 \tag{2}$$

$$\frac{\partial e_e}{\partial t} + \nabla \cdot [\mathbf{v}(e_e + p_e)] - \nabla \lambda_e \nabla T_e + Q_{\mathrm{rad}} + Q_J + Q_{ei} - Q'_m = 0 \tag{3}$$

$$\frac{\partial e_i}{\partial t} + \nabla \cdot [\mathbf{v}(e_i + p_i)] - \nabla \lambda_i \nabla T_i - Q_{ei} = 0 \tag{4}$$

$$\frac{\partial \mathbf{B}}{\partial t} + \nabla \cdot (\mathbf{v}\mathbf{B} - \mathbf{B}\mathbf{v}) + \frac{c^2}{4\pi\mu} \nabla \times (\eta \nabla \times \mathbf{B}) + Q_m = 0 \tag{5}$$

These equations represent the conservation of mass, momentum, energy of electrons, energy of ions, and magnetic flux, respectively. The variables are the mass density (ρ), momentum density ($\rho\mathbf{v}$), internal energy density (e_e) of electrons and (e_i) of ions, and the magnetic field (**B**). The magnetic permeability (μ) was assumed to be 1. The total pressure has hydrodynamic and magnetic components in this formulation:

$$p_{\text{tot}} = p_h + \frac{\mathbf{B}^2}{8\pi} = p_e + p_i + \frac{\mathbf{B}^2}{8\pi} \tag{6}$$

To complete this full set of MHD equations, functions for the thermodynamic pressure of electrons $p_e = p(e_e, \rho)$, resistivity $\eta = \eta(e_e, \rho)$, and thermal conductivity $\lambda_{e/i} = \lambda(e_{e/i}, \rho)$ are determined from the equation of state, discussed below.

Because the LPP device has cylindrical symmetry, the set of Eqs. (1)–(5) was adapted for 2-D cylindrical targets. Plasma motion along the ϕ axis is not considered in this model, and the magnetic field has only one component, B_ϕ. Therefore, to simplify the expressions, subscript ϕ of the magnetic field component is omitted from the magnetic field term. Moreover, the general solution of Eqs. (1)–(5) was separated into two stages: convective and dissipative. The convective stage provides an ideal MHD system solution, where only convective fluxes are present. This stage is given by

$$\frac{\partial \mathbf{U}}{\partial t} + \frac{1}{r}\frac{\partial}{\partial r}[r\mathbf{F}(\mathbf{U})] + \frac{\partial \mathbf{P}(\mathbf{U})}{\partial r} + \frac{\partial \mathbf{G}(\mathbf{U})}{\partial z} = \mathbf{\Omega} \tag{7}$$

where

$$\mathbf{U} = \begin{bmatrix} \rho \\ \rho v^r \\ \rho v^z \\ e_e \\ e_i \\ B \end{bmatrix} \quad \mathbf{F}(\mathbf{U}) = \begin{bmatrix} \rho v^r \\ \rho v^r v^r \\ \rho v^z v^r \\ v^r(e_e + p_e) \\ v^r(e_i + p_i) \\ 0 \end{bmatrix} \quad \mathbf{P}(\mathbf{U}) = \begin{bmatrix} 0 \\ p_{\text{tot}} \\ 0 \\ 0 \\ 0 \\ v^r B \end{bmatrix}$$

$$\mathbf{G}(\mathbf{U}) = \begin{bmatrix} \rho v^z \\ \rho v^r v^z \\ \rho v^z v^z + p_{\text{tot}} \\ v^z(e_e + p_e) \\ v^z(e_i + p_i) \\ v^z B \end{bmatrix} \tag{8}$$

$$\mathbf{\Omega} = \begin{bmatrix} 0 \\ -\dfrac{B^2}{4\pi r} \\ 0 \\ Q_{\text{las}} + Q_{\text{rad}} + Q_{e,\text{th}} + Q_J - Q_{\text{ei}} - Q_m \\ Q_{i,\text{th}} + Q_{\text{ei}} \\ Q_{\text{dif}} + Q_{\text{ms}} \end{bmatrix} \tag{9}$$

The source vector Ω combines several dissipative terms (sources): laser heat Q_{las}, radiation transport Q_{rad}, thermal conductivity Q_{th}, magnetic diffusion Q_J and Q_{dif}, magnetic source Q_m and Q_{ms}, and electron–ion interactions Q_{ei}. The terms are calculated with the second (dissipative) stage of the HEIGHTS solver and are used as correctors of the main convective solution. The conservative form of the initial equations allows the use of the TVD method [6, 7] in the Lax-Friedrich formulation (TVD-LF) for solution of the convective stage given by Eq. (7). A second-order TVD-LF scheme does not use a Riemann solver and can be applied to the conservation laws without knowledge of the characteristic waves. The matrix formalism enables us to change the governing Eq. (7) without significantly modifying the method. For example, to obtain the two-temperature approximation, the total energy equation [3, 4] were split, and the elements of the matrixes were extended to six.

The initial physical model of the LPP device includes a laser heat term of the electron gas (Q_{las} term). The electron gas yields the spatial temperature gradient, which can be nonparallel to the electron concentration gradient. This condition is necessary for magnetic field generation: the internal energy of the electron gas is dissipative (Q_m term) because of the magnetic field creation (Q_{ms} term). The magnetic field generation is equivalent to the plasma internal current produced. The generated currents heat the electron gas (return energy back) in the Joule heating process (Q_J), which can be expressed as magnetic field diffusion (Q_{dif} term in magnetic field equation). The model is completed with the thermal electron–ion interactions, which include the energy exchange between the electron and ion gases (Q_{ei} term). Thermal conduction processes in electron ($Q_{e,\text{th}}$) and ion ($Q_{i,\text{th}}$) gases are also included. The radiation transport model describes the energy redistribution in the electron gas (Q_{rad} term) and completes the physical model.

Laser energy deposition is mainly by the inverse bremsstrahlung, since we are assuming the initial preheating of the target is to 1 eV. In the results reported here, the classical absorption coefficient (corrected in [13]) was used:

$$K_{\text{BS}} = \frac{16\pi Z^2 n_e n_i e^6 \ln\Lambda}{3c\nu^2 (2\pi m_e k_B T_e)^{3/2} (1 - \nu_p^2/\nu^2)^{1/2}} \tag{10}$$

where n_e, n_i are the electron and ion concentrations; e is electron charge; Ze is average ionic charge; c is light speed; m_e is electron mass; k_B is the Boltzmann constant; T_e is electron gas temperature; ν_P is plasma frequency; and ν is laser radiation frequency [14]. The Coulomb logarithm $\ln\Lambda$ is given by [15]

$$\ln\Lambda = \ln\left[\frac{3}{2}\sqrt{\frac{(k_B T_e)^3}{\pi n_e}}\frac{1}{Ze^3}\right] \tag{11}$$

Reflection of the laser radiation was simulated in the plasma when the plasma frequency ν_P equals the arrived frequency of laser light. Heat conduction in the electron and ion gases included dependence of the coefficients of thermal conductivity

on the magnetic field [16]:

$$\lambda_e = \frac{25 n_i T_e k_B^2}{4\beta_e \gamma_e m_e} \frac{1}{1 + (25\Omega_e^2)/[\beta_e(4\beta_e - 9)\gamma_e^2]} \qquad \lambda_i = \frac{25 n_i T_i k_B^2}{4\beta_i \gamma_i m_i} \frac{1}{1 + (6.25\Omega_i^2)/(\beta_i^2 \gamma_i^2)} \tag{12}$$

where

$$\gamma_e = \frac{4\sqrt{2\pi} e^4 n_i \ln\Lambda}{3(k_B T_e)^{3/2} m_e^{1/2}} \qquad \gamma_i = \frac{4\sqrt{2\pi} e^4 n_i \ln\Lambda}{3(k_B T_i)^{3/2} m_i^{1/2}} \tag{13}$$

$$\beta_e = \sqrt{2} + \frac{13}{4} \qquad \beta_i = \sqrt{2} + \frac{15}{2}\left(\frac{T_i}{T_e}\right)^{3/2}\left(\frac{m_e}{m_i}\right)^{1/2} \tag{14}$$

with magnetic field dependences of the cyclotron frequencies $\Omega_{e/i} = eB/cm_{e/i}$.

The magnetic source term [17, 18],

$$Q_{ms} = -\frac{ck_B}{en_e} \nabla n_e \times \nabla T_e$$

was transformed for the cylindrical case:

$$Q_{ms} = \frac{ck_B}{en_e}\left(\frac{\partial n_e}{\partial r}\frac{\partial T_e}{\partial z} - \frac{\partial n_e}{\partial z}\frac{\partial T_e}{\partial r}\right) \tag{15}$$

The decreasing electron internal energy Q_m can be calculated from the assumption that energy of the magnetic field is $e_m = B^2/8\pi$. The magnetic diffusion and Joule heating were determined with the Spitzer resistivity expression [15],

$$\eta = \frac{1}{2}\sqrt{\frac{\pi^3 m_e}{8(k_B T_e)^3}} Z e^2 \ln\Lambda \tag{16}$$

The Joule heating term in the 2-D cylindrical symmetry case taking into account Eq. (16) can be written as

$$Q_J = \frac{c^2 \eta}{16\pi^2}\left[\frac{1}{r^2}\left(\frac{\partial rB}{\partial r}\right)^2 + \left(\frac{\partial B}{\partial z}\right)^2\right] \tag{17}$$

The electron-ion energy exchange was considered as a function of electron and ion gas temperatures [14, 19]:

$$Q_{\mathrm{ei}} = 3\frac{m_e n_e}{m_i \tau_e}(k_B T_e - k_B T_i) \tag{18}$$

where the time between electron interactions is

$$\tau_e = \frac{3\sqrt{m_e}(k_B T_e)^{3/2}}{4\sqrt{2\pi} e^4 Z^2 n_i \ln\Lambda} \tag{19}$$

The Monte Carlo radiation transport model has been described in detail [5]. Additionally, we note good applicability of this method to LPP radiation transport

where two extreme cases are present: an optically ''thick'' and ''thin'' plasma. The developed weight factors method helps avoid difficulties associated with transport calculations of an inhomogeneous medium.

NUMERICAL METHOD

The convective stage is handled by the ideal MHD system solution, where only convective fluxes are present. The TVD mechanism was used for calculations of the convective part. The numerical scheme based on the TVD-LF method is given in [3, 5]. We describe in this article the dissipative stage of the combined solution, where the heat transport and magnetic diffusion terms are included as Q sources in the Ω vector of Eq. (7). In analogy to [20], an implicit method on the base of sparse matrixes was developed for these equations. We used a grid of gradually varying cell size by imposing unequal grid spacing $\Delta r_i = r_{i+1/2} - r_{i-1/2}$ and $\Delta z_j = z_{j+1/2} - z_{j-1/2}$ in the r and z directions, respectively. The subscripts $i + 1/2$ and $j + 1/2$ refer to quantities defined on the cell interfaces $r_{i+1/2}$ and $z_{j+1/2}$. Cell centers $r_i = (r_{i+1/2} + r_{i-1/2})/2$ and $z_j = (z_{j+1/2} + z_{j-1/2})/2$ are specified at positions (i, j). We used standard notations for evaluating functions $T^n_{i,j}$ and $B^n_{i,j}$ defined at cell centers (i, j) and time level n. We assumed time spacing t^n with intervals $\Delta t^n = t^{n+1} - t^n$. The spatial derivatives were approximated at each point (i, j) using centered differences with truncation error of order $o = 2$.

The heat conduction equation is given in accepted symbols as

$$\frac{\partial}{\partial t}\rho c_p T(t,r,z) - \frac{1}{r}\frac{\partial}{\partial r} r\lambda \frac{\partial}{\partial r} T(t,r,z) - \frac{\partial}{\partial z}\lambda \frac{\partial}{\partial z} T(t,r,z) = 0 \tag{20}$$

The plasma properties are assumed to be constant during each time step. This assumption allows us to consider the first term in Eq. (20) as a constant source, like Poisson's equation. We next assumed finite-difference approximations for the derivation construction replacements:

$$\left[\frac{1}{r}\frac{\partial}{\partial r} r\lambda \frac{\partial}{\partial r} T(t,r,z)\right]_{i,j} = C^r_1 T_{i-1,j} + C^r_2 T_{i,j} + C^r_3 T_{i+1,j} \tag{21}$$

where

$$\begin{aligned} C^r_1 &= \frac{2\lambda_{i-1/2,j} r_{i-1/2}}{r_i \Delta r_i (\Delta r_{i-1} + \Delta r_i)} \\ C^r_2 &= -\frac{2[\lambda_{i+1/2,j} r_{i+1/2}(\Delta r_{i-1} + \Delta r_i) + \lambda_{i-1/2,j} r_{i-1/2}(\Delta r_{i+1} + \Delta r_i)]}{r_i \Delta r_i (\Delta r_{i-1} + \Delta r_i)(\Delta r_{i+1} + \Delta r_i)} \\ C^r_3 &= \frac{2\lambda_{i+1/2,j} r_{i+1/2}}{r_i \Delta r_i (\Delta r_{i+1} + \Delta r_i)} \end{aligned} \tag{22}$$

Plasma properties on the cell borders are calculated by linear interpolation:

$$\lambda_{i+1/2,j} = \frac{\Delta r_i \lambda_{i+1,j} + \Delta r_{i+1} \lambda_{i,j}}{\Delta r_i + \Delta r_{i+1}} \tag{23}$$

Derivation in the z direction is given by

$$\left[\frac{\partial}{\partial z}\lambda\frac{\partial}{\partial z}T(t,r,z)\right]_{i,j} = C_1^z T_{i,j-1} + C_2^z T_{i,j} + C_3^z T_{i,j+1} \tag{24}$$

where

$$\begin{aligned} C_1^z &= \frac{2\lambda_{i,j-1/2}}{\Delta z_j(\Delta z_{j-1}+\Delta z_j)} \\ C_2^z &= -\frac{2[\lambda_{i,j+1/2}(\Delta z_{j-1}+\Delta z_j)+\lambda_{i,j-1/2}(\Delta z_{j+1}+\Delta z_j)]}{\Delta z_j(\Delta z_{j-1}+\Delta z_j)(\Delta z_{j+1}+\Delta z_j)} \\ C_3^z &= \frac{2\lambda_{i,j+1/2}}{\Delta z_j(\Delta z_{j+1}+\Delta z_j)} \end{aligned} \tag{25}$$

Application of Eqs. (21) and (24) allows the heat conduction Eq. (20) to be presented as a set of linear equations, where the total number of equations is equivalent to the total number of useful cells in the domain:

$$A_{i-1,j}T_{i-1,j}^{n+1} + A_{i,j}T_{i,j}^{n+1} + A_{i+1,j}T_{i+1,j}^{n+1} + A_{i,j-1}T_{i,j-1}^{n+1} + A_{i,j+1}T_{i,j+1}^{n+1} = D_{i,j} \tag{26}$$

Substitution of Eqs. (21) and (24) into (20) yields linear coefficients A and D for the heat conduction equation:

$$\begin{aligned} &A_{i-1,j} = C_1^r, \qquad A_{i,j} = C_2^r + C_2^z - \frac{c_{p\{i,j\}}^n \rho_{i,j}^n}{\Delta t^n} \qquad A_{i+1,j} = C_3^r, A_{i,j-1} = C_1^z \\ &A_{i,j+1} = C_3^z \qquad D_{i,j} = -\frac{c_{p\{i,j\}}^n \rho_{i,j}^n T_{i,j}^n}{\Delta t^n} \end{aligned} \tag{27}$$

It was assumed that the plasma parameters do not change during one time step; linear equations include specific heat $c_{p\{i,j\}}^n$ and density $\rho_{i,j}^n$ with n time steps. Equation (26) is a closed system in which the number of unknown values equals the number of linear equations if the boundary conditions are determined. The temperature function has no singularity at point $r = 0$, and the equivalence $(\partial T/\partial r)|_{r=0} = 0$ can be taken as a boundary condition by using the symmetry axis as the domain border.

In general, boundary conditions on any border Γ are given by $\alpha\lambda\nabla T|_\Gamma + \beta T|_\Gamma = f(T|_\Gamma, t)$, where the numerical parameters α and β can specify the situation at the Γ border as given heat flux ($\alpha = 1$, $\beta = 1$), given temperature ($\alpha = 0$, $\beta = 1$), or heat flux as a function of temperature. The simplest case of thermally isolated borders can be realized for the cylindrical geometry as equivalences $(\partial T/\partial r)|_{\Gamma(r=\text{const})} = 0$ and $(\partial T/\partial z)|_{\Gamma(z=\text{const})} = 0$. A more comprehensive discussion of boundary condition is presented in [21].

Numerical simulation with the implicit scheme is unconditionally stable, and by using combined schemes, the limiting factor on the time step is usually the explicit part (convection stage in our case). Ideal MHD calculations demand Courant-Friedrich-Levi conditions for that explicit algorithm [22]. As the heat conduction equation, the time-step limiter can be used, $\Delta t \sim \min|(\Delta x^2 c_p \rho/2\lambda)|$, where Δx is the minimal cell size.

The magnetic diffusion equation has several exceptions in the finite-difference scheme. One concerns the behavior of mesh function near the r zero point. The general structures of the heat conduction and magnetic diffusion equations

are similar:

$$\frac{\partial}{\partial t}B(t,r,z)-\frac{\partial}{\partial r}\frac{c^2\eta}{4\pi r}\frac{\partial}{\partial r}rB(t,r,z)-\frac{\partial}{\partial z}\frac{c^2\eta}{4\pi}\frac{\partial}{\partial z}B(t,r,z)=0 \tag{28}$$

Similar to Eq. (21), the second term in Eq. (28) is given by

$$\left[\frac{\partial}{\partial r}\frac{\eta}{r}\frac{\partial}{\partial r}rB(t,r,z)\right]_{i,j}=C_1^rB_{i-1,j}+C_2^rB_{i,j}+C_3^rB_{i+1,j} \tag{29}$$

where

$$\begin{aligned}
C_1^r&=\frac{2\eta_{i-1/2,j}r_{i-1}}{r_{i-1/2}\,\Delta r_i(\Delta r_{i-1}+\Delta r_i)}\\
C_2^r&=-\left[\frac{2\eta_{i+1/2,j}r_i}{r_{i+1/2}\,\Delta r_i(\Delta r_i+\Delta r_{i+1})}+\frac{2\eta_{i-1/2,j}r_i}{r_{i-1/2}\,\Delta r_i(\Delta r_{i-1}+\Delta r_i)}\right]\\
C_3^r&=\frac{2\eta_{i+1/2,j}r_{i+1}}{r_{i+1/2}\,\Delta r_i(\Delta r_i+\Delta r_{i+1})}\qquad \text{for } r_{i-1/2}\neq 0,\ \text{i.e., } i>1
\end{aligned} \tag{30}$$

The requirement of the equivalence of left- and right-side derivatives and the calculation of the limit to zero yield a full description of numerical function behavior near the singularity point $B|_{r=0}=0$,

$$\begin{aligned}
\left.\frac{\partial B}{\partial r}\right|_+&=-\left.\frac{\partial B}{\partial r}\right|_-\\
\lim_{r\to 0}\frac{c^2\eta}{4\pi\mu r}\frac{\partial rB}{\partial r}&=\frac{c^2\eta}{2\pi\mu}\lim_{r\to 0}\frac{\partial B}{\partial r}
\end{aligned} \tag{31}$$

Implementation of Eq. (31) conditions into (29) provides coefficients for the first cell:

$$\begin{aligned}
&C_1^r=0\qquad C_2^r=-\left[\frac{2\eta_{3/2,j}r_1}{r_{3/2}\,\Delta r_1(\Delta r_1+\Delta r_2)}+\frac{4\eta_{1/2,j}}{\Delta r_1^2}\right]\\
&C_3^r=\frac{2\eta_{3/2,j}r_2}{r_{3/2}\,\Delta r_1(\Delta r_1+\Delta r_2)}\qquad \text{for } i=1
\end{aligned} \tag{32}$$

The z-axis term in the magnetic diffusion equation (28) has no exclusions and can be derived similarly to heat conduction:

$$\left[\frac{\partial}{\partial z}\eta\frac{\partial}{\partial z}B(t,r,z)\right]_{i,j}=C_1^zB_{i,j-1}+C_2^zB_{i,j}+C_3^zB_{i,j+1} \tag{33}$$

where

$$\begin{aligned}
C_1^z&=\frac{2\eta_{i,j-1/2}}{\Delta z_j(\Delta z_{j-1}+\Delta z_j)}\\
C_2^z&=-\frac{2\left[\eta_{i,j+1/2}(\Delta z_{j-1}+\Delta z_j)+\eta_{i,j-1/2}(\Delta z_{j+1}+\Delta z_j)\right]}{\Delta z_j(\Delta z_{j-1}+\Delta z_j)(\Delta z_{j+1}+\Delta z_j)}\\
C_3^z&=\frac{2\eta_{i,j+1/2}}{\Delta z_j(\Delta z_{j+1}+\Delta z_j)}
\end{aligned} \tag{34}$$

Finally, after transformations, the magnetic diffusion equation (28) can be represented as a linear equation system:

$$A_{i-1,j}B^{n+1}_{i-1,j} + A_{i,j}B^{n+1}_{i,j} + A_{i+1,j}B^{n+1}_{i+1,j} + A_{i,j-1}B^{n+1}_{i,j-1} + A_{i,j+1}B^{n+1}_{i,j+1} = D_{i,j} \tag{35}$$

where coefficients A and D are calculated from corresponding the C:

$$\begin{aligned} A_{i-1,j} &= C^r_1 \qquad A_{i,j} = C^r_2 + C^z_2 - \frac{4\pi\mu}{\Delta t^n c^2} \qquad A_{i+1,j} = C^r_3 \\ A_{i,j-1} &= C^z_1 \qquad A_{i,j+1} = C^z_3 \\ D_{i,j} &= -\frac{4\pi\mu B^n_{i,j}}{\Delta t^n c^2} \end{aligned} \tag{36}$$

In the heat conduction case, plasma properties on the cell borders are calculated by linear interpolation of Eq. (23). Discussion of time steps for implicit magnetic diffusion algorithms can be found in [23].

Conditions on the external borders of the domain are determined with physical processes. Most useful are: current $B|_\Gamma = 2I/rc$; symmetry $(\partial rB/\partial r)|_{\Gamma(r=\text{const})} = 0$, $\partial B/\partial z|_{\Gamma(z=\text{const})} = 0$; and conducting wall $B|_\Gamma = 0$.

Finally, Eqs. (26) and (35) can be expressed in matrix form as $\mathbf{A}\cdot\mathbf{U} = \mathbf{D}$, where $\mathbf{A}$ and $\mathbf{D}$ are matrixes of coefficients A and D, and $\mathbf{U}$ is a matrix of unknown field ($T^{n+1}_{i,j}$ or $B^{n+1}_{i,j}$). We present the matrix expression for the heat conduction equation in the $n \times m$ domain where zero elements are indicated. The linear system is sparse and five-diagonal. The coefficient matrix is $n{\cdot}m \times n{\cdot}m$. In our LPP problem, the largest grid size was 100 $\times$ 200 cells, which produces a coefficient matrix of about 4.0×10^8 elements. It is a large sparse matrix containing an extremely large numbers of zero elements:

$$\begin{bmatrix} A_{1,1} & A_{2,1} & 0 & 0 & \cdots & A_{1,2} & 0 & 0 & 0 & 0 & 0 \\ A_{1,1} & A_{2,1} & A_{3,1} & 0 & \cdots & 0 & A_{2,2} & 0 & 0 & 0 & 0 \\ 0 & A_{2,1} & A_{3,1} & A_{4,1} & \cdots & 0 & 0 & A_{3,1} & 0 & 0 & 0 \\ \cdots & \cdots & \cdots & \cdots & \cdots & \cdots & \cdots & \cdots & \cdots & \cdots & \cdots \\ 0 & \cdots & A_{i,j-1} & \cdots & A_{i-1,j} & A_{i,j} & A_{i+1,j} & \cdots & A_{i,j+1} & \cdots & 0 \\ \cdots & \cdots & \cdots & \cdots & \cdots & \cdots & \cdots & \cdots & \cdots & \cdots & \cdots \\ 0 & 0 & 0 & A_{n-2,m-1} & 0 & 0 & \cdots & A_{n-3,m} & A_{n-2,m} & A_{n-1,m} & 0 \\ 0 & 0 & 0 & 0 & A_{n-1,m-1} & 0 & \cdots & 0 & A_{n-2,m} & A_{n-1,m} & A_{n,m} \\ 0 & 0 & 0 & 0 & 0 & A_{n,m-1} & \cdots & 0 & 0 & A_{n-1,m} & A_{n,m} \end{bmatrix}$$

$$\times \begin{bmatrix} T^{n+1}_{1,1} \\ \cdots \\ T^{n+1}_{n,1} \\ T^{n+1}_{1,2} \\ \cdots \\ T^{n+1}_{n,2} \\ \cdots \\ T^{n+1}_{1,m} \\ \cdots \\ T^{n+1}_{n,m} \end{bmatrix} = \begin{bmatrix} D_{1,1} \\ \cdots \\ D_{n,1} \\ D_{1,2} \\ \cdots \\ D_{n,2} \\ \cdots \\ D_{1,m} \\ \cdots \\ D_{n,m} \end{bmatrix} \tag{37}$$

The structure of the matrix is invariable when linear equations that describe nonuseful cells (in the case of the complex domain) are removed. Key to efficiency is to store and operate on only nonzero entries of the matrix. Several mathematic libraries (e.g., NAG, IMSL, and PARDISO) are used for solution of linear equation systems with a band or sparse matrix. Calculations for the complex domain need special code for implementation of boundary conditions and exclusion of nonuseful domain areas. If the computational domain does not change during the simulation time (no motion of any device walls), the best way is to analyze the domain form before the start of the main program, and to prepare templates of needed matrixes. In contrast to the explicit algorithm, where it is possible to have a separate module of boundary conditions, the implicit code requires embedding of the linear coefficients A and D during construction of matrixes **A** and **D**. The dissipative stage fields $\Delta e_{i,j} = \rho_{i,j} c_{p\{i,j\}} \left(T_{i,j}^{n+1} - T_{i,j}^{n} \right)$ and $\Delta B_{i,j} = B_{i,j}^{n+1} - B_{i,j}^{n}$ can be considered as dissipative sources for the ideal MHD solution on each time step. We utilize them as dissipative terms Q in vector Ω on the right side of Eq. (7).

VALIDATION AND BENCHMARKING

To validate the model and benchmark the code, two test problems were solved and compared with known analytical results [24]. The first test problem describes heat transport into the semirestricted computational domain with thermal conductivity $\lambda = \lambda_0 T^{\alpha}$. The power dependence of conductivity allows analytical solution of the heat transport problem

$$\frac{\partial T}{\partial t} = \frac{\partial}{\partial z} \lambda_0 T^{\alpha} \frac{\partial T}{\partial z} \qquad \text{for } z > 0,\ t > 0 \tag{38}$$

with initial and boundary conditions

$$\begin{aligned} T(0,t) &= \left[\frac{\alpha D}{\lambda_0} (z_1 + Dt) \right]^{1/\alpha} && t > 0 \\ T(z,0) &= \begin{cases} \left[\dfrac{\alpha D}{\lambda_0} (z_1 - z) \right]^{1/\alpha} & 0 < z \le z_1 \\ 0 & z > z_1 \end{cases} \end{aligned} \tag{39}$$

given by

$$T(z,t) = \begin{cases} \left[\dfrac{\alpha D}{\lambda_0} (Dt + z_1 - z) \right]^{1/\alpha} & 0 < z \le z_1 + Dt \\ 0 & z > z_1 + Dt \end{cases} \tag{40}$$

Test calculations were performed for the parameter set $\alpha = 2$, $\lambda_0 = 0.5$, $z_1 = 0$, and $D = 5$ on uniform and appreciably nonuniform meshes. Figure 2 presents time-step calculations for the implicit algorithm with uniform mesh and $\Delta z = 10^{-2}$. The heat front at time moment $t = 0.1$ is shown. The scheme remains stable for very large time steps. Analytical results and numerical simulation

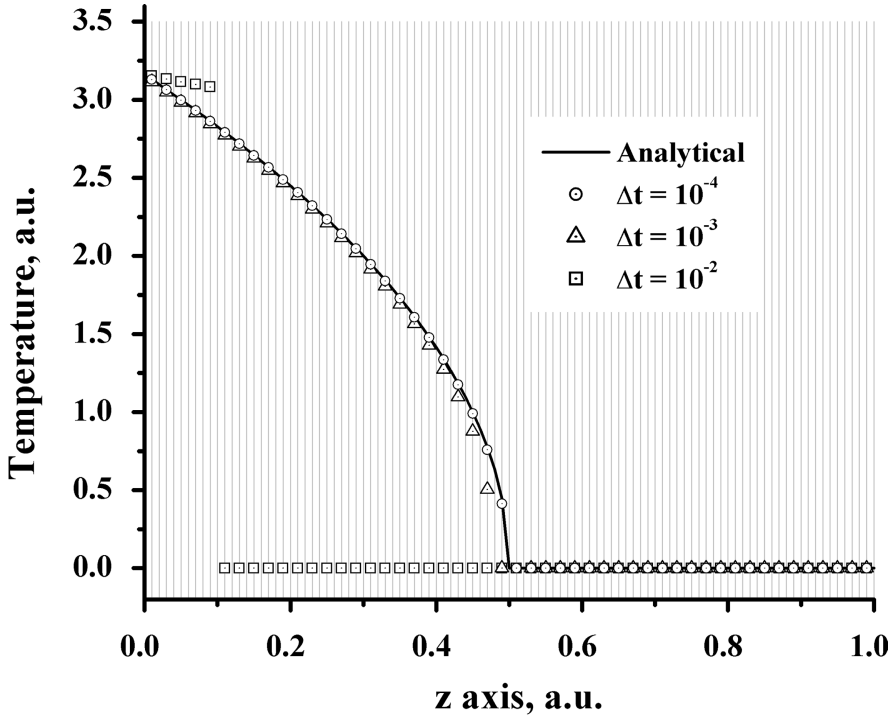

Figure 2. Heat front distribution calculated with different time steps. Uniform mesh $\Delta z = 0.01$. Time moment $t = 0.1$.

solutions for this heat transport problem were satisfactorily fit by $\Delta t \leq 10^{-4}$ with the implicit method. We also constructed a simple explicit numerical scheme and obtained similar results to the implicit scheme but only by using time steps smaller than $\Delta t \leq 10^{-6}$. Larger time steps caused oscillations and numerical scheme disturbances. Accordingly, the difference between implicit and explicit time steps is two orders of magnitude.

The implicit algorithm retains stability by using the appreciably nonuniform meshes. The evolution of the heat front on nonuniform mesh is presented in Figure 3. The calculations carried out with time step $\Delta t = 10^{-4}$. The analytical and numerical simulation results compare very well.

The second numerical test investigated the "stopped" temperature wave, which can be obtained from Eq. (38) at intervals $z > 0$, and $0 < t < C$ with initial and boundary conditions given by

$$
\begin{aligned}
T(0,t) &= \left[\frac{\alpha z_1}{2\lambda_0(\alpha+2)(C-t)}\right]^{1/\alpha} \qquad 0 < t < C \\
T(z,0) &= \begin{cases} \left[\dfrac{\alpha(z_1-z)^2}{2\lambda_0(\alpha+2)C}\right]^{1/\alpha} & 0 < t < C \\ 0 & z > z_1 \end{cases}
\end{aligned}
\tag{41}
$$

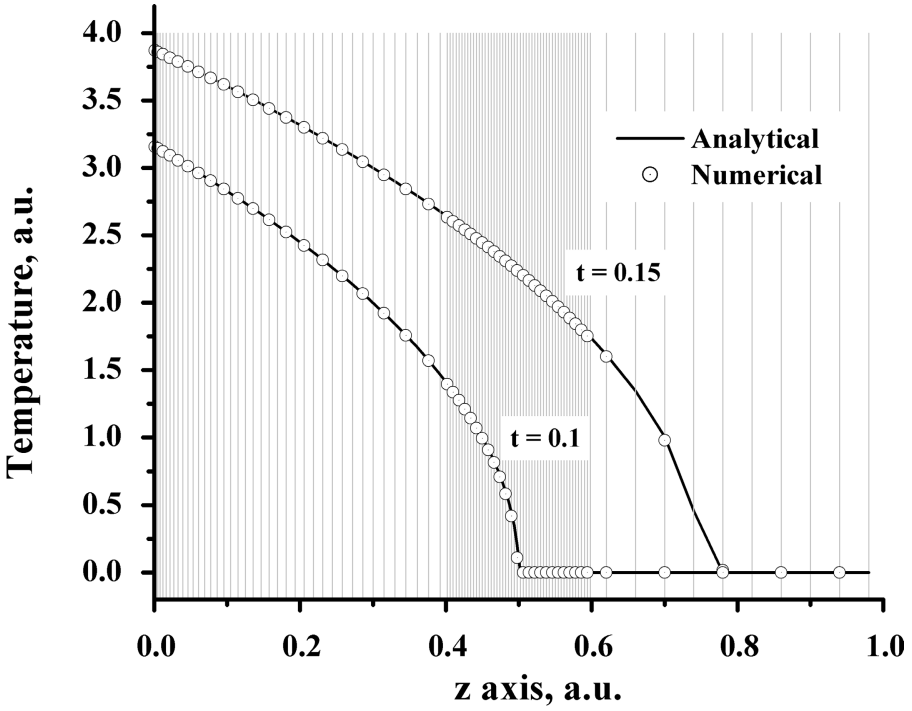

Figure 3. Heat front evolution. Nonuniform mesh; time step $\Delta t = 10^{-4}$.

The temperature-front evolution in this case is

$$T(z,t) = \begin{cases} \left[\dfrac{\alpha(z_1 - z)^2}{2\lambda_0(\alpha+2)(C-t)}\right]^{1/\alpha} & 0 \le z \le z_1 \\ 0 & z > z_1 \end{cases} \tag{42}$$

Analytical and numerical simulation results were compared for coefficients $\alpha = 2$, $\lambda_0 = 0.5$, $z_1 = 0.5$, and $C = 0.1125$. Figure 4 presents calculations obtained by an implicit scheme with time step $\Delta t = 10^{-4}$ on uniform spatial mesh $\Delta z = 10^{-4}$.

Our validation of the numerical simulations with analytical results showed stability and accuracy for artificial problems. However, computation for real devices is of much more interest in method application. We thus compared results for a discharge plasma device calculated by both implicit and explicit schemes. A detailed description of the discharge device is given in [5]. Figure 5 includes temperature and magnetic field distributions around the device electrode at 200 ns after discharge start. The computational procedure combined magnetic field input with external current and excluded the electrode area from the domain. The plasma motion was calculated by the implicit scheme and by substitution of heat and magnetic diffusion fluxes directly into the MHD explicit scheme [3, 4]. The results obtained by both schemes compared well. Figure 6 shows crosssections of temperature and magnetic

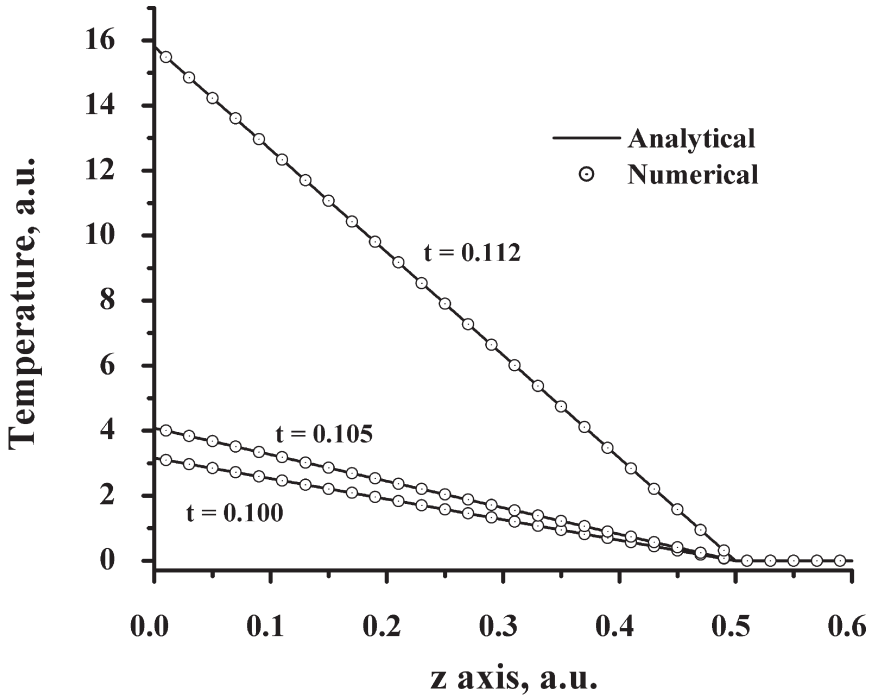

Figure 4. "Stopped" temperature wave. Time step $\Delta t = 10^{-4}$. Uniform mesh $\Delta t = 10^{-2}$.

fields distributions calculated by both schemes for $z = 1.5$ cm in Figure 5. The independent implicit scheme has a number of advantages over the direct MHD explicit method. Of vital importance is the ability to use much longer time steps. The curves

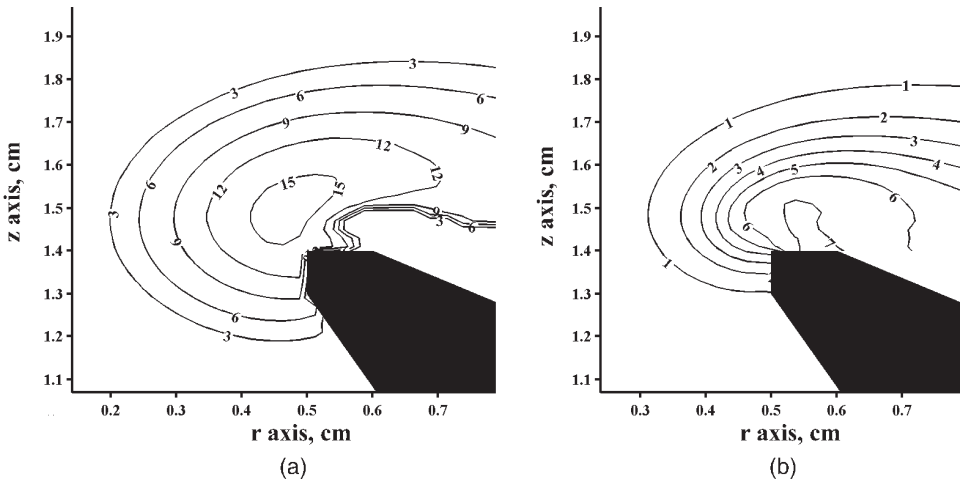

Figure 5. Plasma parameter distributions around electrode at $t = 200$ ns: (*a*) temperature field (eV); (*b*) magnetic field (kG).

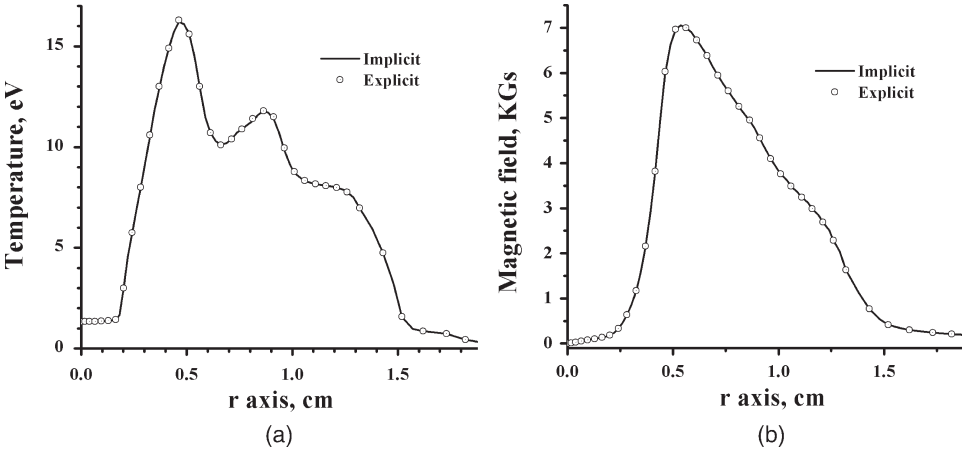

Figure 6. Plasma parameter distributions along R axis at $t = 200$ ns: (*a*) temperature field (eV); (*b*) magnetic field (kGs).

in Figure 6 were calculated with time step $\Delta t = 5$ ps for the implicit method and $\Delta t = 5 \times 10^{-2}$ ps for the explicit method. The time step is strongly confined with heat transport in areas of small plasma density. These areas are usually the back of the magnetic "snow plow."

The explicit scheme is very unstable in heat transport calculations for rarefied plasma. Physically, it is possible to explain by consideration of the mechanism of the thermal conductivity: hot particles transfer energy into neighbor cells, as a result of chaotic thermal motions.

The explicit scheme works well if the particles can arrive and exchange energy in the adjacent cells only during one time step. This scheme is not able to consider energy redistribution in the next nearest cells. The consecutive energy transport is taken into account. The frequency of particle interactions declines by decreasing of density, and the time of flight through the cell is appreciably shorter. The explicit scheme includes nonuseful time steps in the case described. This is related to the physical concept of the Courant-Friedrich-Levy (CFL) conditions. A similar unstable situation takes place by consideration of magnetic diffusion during the stage of plasma compression near the zero point on the radial axis [25].

Additional procedures are needed for damping nonphysical oscillations in the explicit case. The explicit method allowed us to simulate plasma motion in discharge-produced plasma devices of several constructions [5]. We note the stability of the numerical algorithm in combination with other processes of energy or magnetic field transport, such as radiation transport, thermomagnetic source, and laser beam interactions.

RESULTS AND DISCUSSION

The energy of the laser pulse was assumed to be 120 mJ, delivered in 10 ns within a 50-μm-diameter focal spot using 1.053-μm-wavelength light. Calculations were performed for uniform (square) time and space distributions of the laser energy

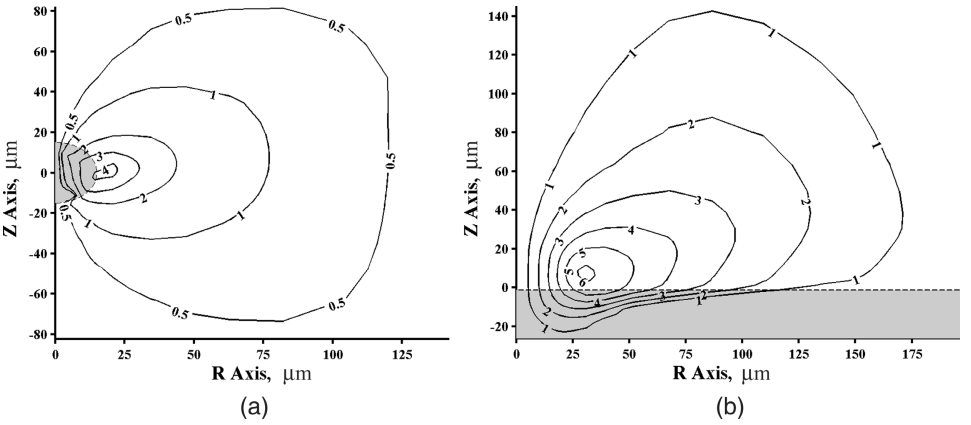

Figure 7. Generated magnetic field distribution (kGs) at $t = 1$ ns: (*a*) Xe droplet ($d = 30$ μm) target; (*b*) Xe planar target.

pulse. The power density derived from these parameters is 6.0×10^{11} W/cm^2. So a comparable high intensity was used to estimate the influence of the generated magnetic field on the plasma evolution and on EUV generation. Figure 7 presents the magnetic field distributions for Xe targets: (*a*) 30-μm target droplet and (*b*) planar target at 1 ns after laser pulse start. The gray filling shows initial borders for the targets. Laser beam direction corresponds to Figure 1. The magnetic field maximum is near 4–6 kGs, and this value will decrease with time. Calculations without taking into account magnetic field generation were also done. Comparison of the plasma parameter evolution in both cases revealed that the generated magnetic field does not account for the visible changes of the plasma temperature, density, and velocity. Correspondingly, magnetic source and magnetic field equations can be omitted by consideration of EUV generation with laser power density $\sim 10^{11}$ W/cm^2. The MHD code can be reconstructed for more efficient working by reduction of the rank for the operating matrixes.

The EUV radiation was registered within a 2% bandwidth at 13.5 nm. Figure 8 presents typical EUV flux distributions around the droplet Xe and Sn targets. Also shown are the density distributions at the same time point (9 ns). As expected, the tin target has higher flux field for the EUV radiation. The time evolution of EUV output is presented in Figure 9 for droplet targets. The radiation energy was recorded for the 2π sr solid angle from the laser beam direction. Time integration of the Figure 9 curves gives the total EUV energy that can be radiated in 2π sr during one laser pulse. This value is 0.485 mJ for the xenon target and 1.252 mJ for the tin target. Integration shows that tin is more effective under selected conditions by a factor of 2.5.

Figure 10 shows the EUV flux distribution for the planar case. The curves indicate that smaller fluxes can be compensated with larger radiated area. Integration by time in 2π sr gives 0.958 mJ for the Xe target. In contrast to the models which are now being used for EUV study of LPP devices [26–28], our calculations indicate a multidimensional character to the plasma radiation processes. The planar target case

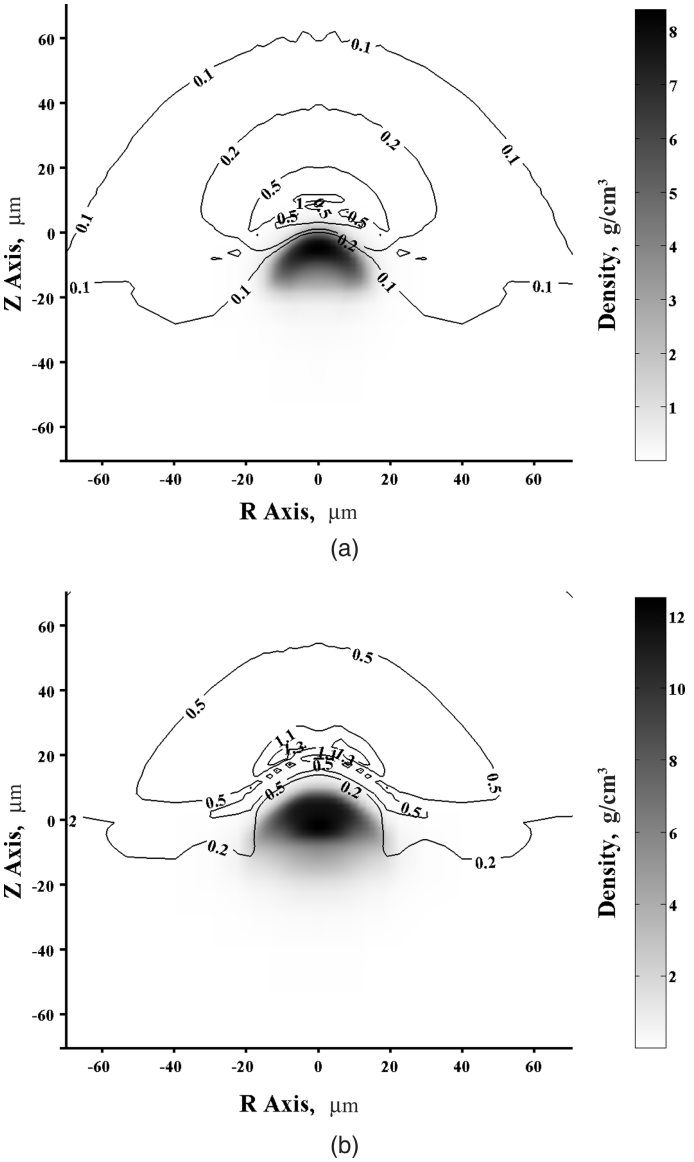

Figure 8. EUV in band flux field (GW/cm^2) at $t = 9$ ns: (*a*) Xe droplet ($d = 36$ μm) target; (*b*) Sn droplet ($d = 36$ μm) target.

indicates EUV output increasing around the laser spot. In contrast, the droplet target case shows the EUV radiation peak located in the center of the laser beam axis. The plasma medium radiates effectively in the restricted spectral band if density and temperature are optimal. The plasma properties for the LPP device satisfy these conditions in other places, depending on the target geometry and on the laser-radiation power density distribution in the laser beam.

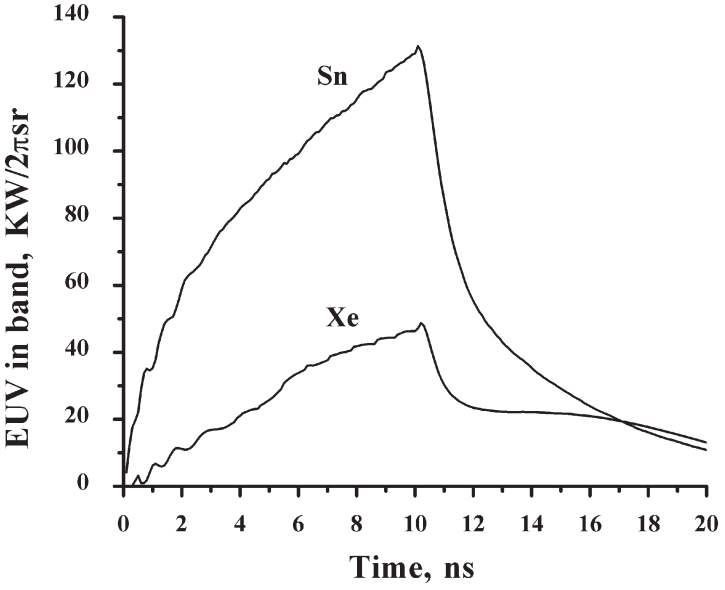

Figure 9. EUV in band output into 2π sr solid angle. Time curves for droplet ($d = 36\,\mu$m) targets.

The most interesting information for lithography concerns the location and size of the EUV source. These parameters can be determined from the space distribution of the EUV power capability in the plasma. The EUV power capability is the radiation in the band output (2π sr solid angle) related to volume unit. Integration by pinch time and plasma space gives the full EUV energy that can be collected from the

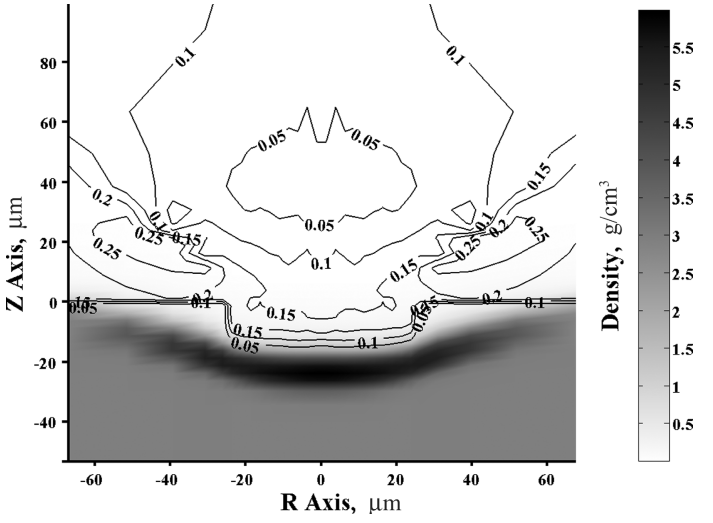

Figure 10. EUV in band flux field (GW/cm^2) at $t = 9$ ns for Xe planar target.

source in 2π sr. Figure 11 depicts EUV power capability, electron temperature, and density along the Z axis (laser beam axis). As shown, the EUV source is a very thin layer near the current edge of the target. The layer moves during the laser pulse, and

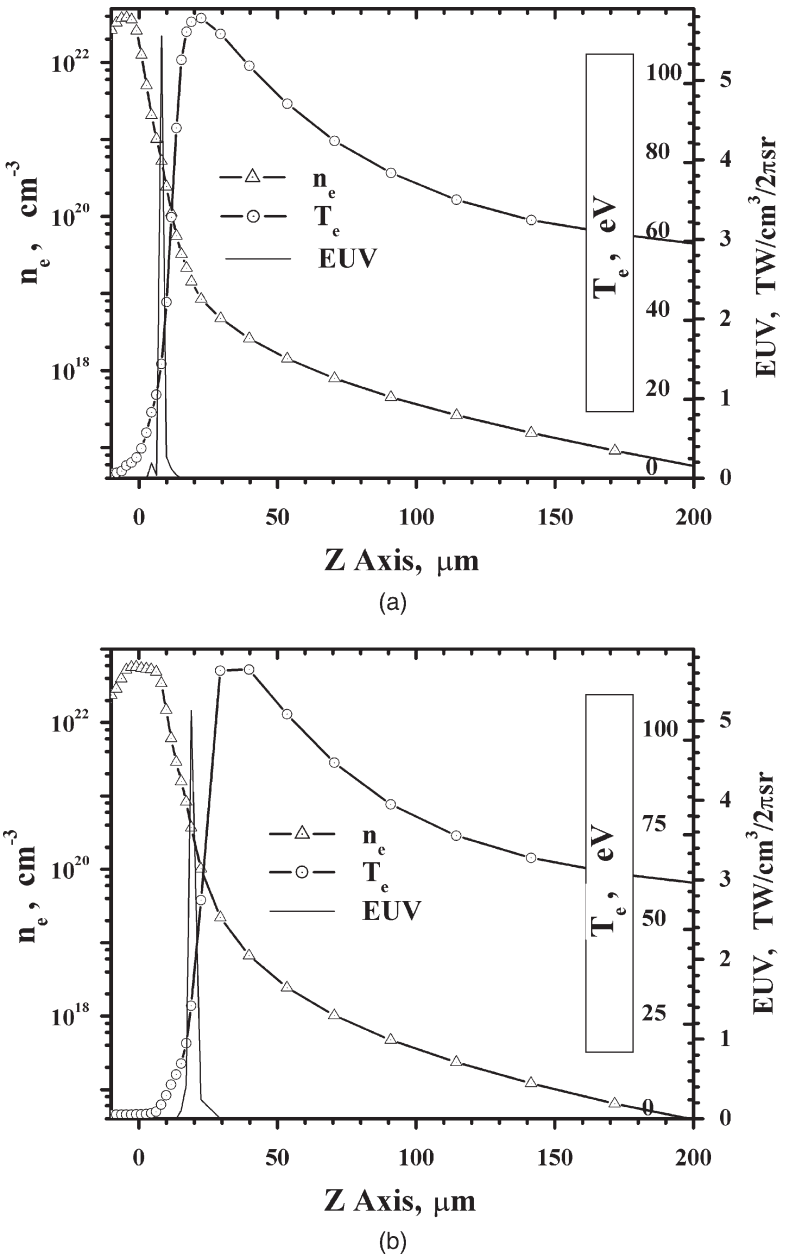

Figure 11. Electron concentration (n_e), electron temperature (T_e), and EUV capability of space along Z axis at $t = 9$ ns after irradiation start: (*a*) Xe droplet ($d = 36\,\mu$m) target; (*b*) Sn droplet ($d = 36\,\mu$m) target.

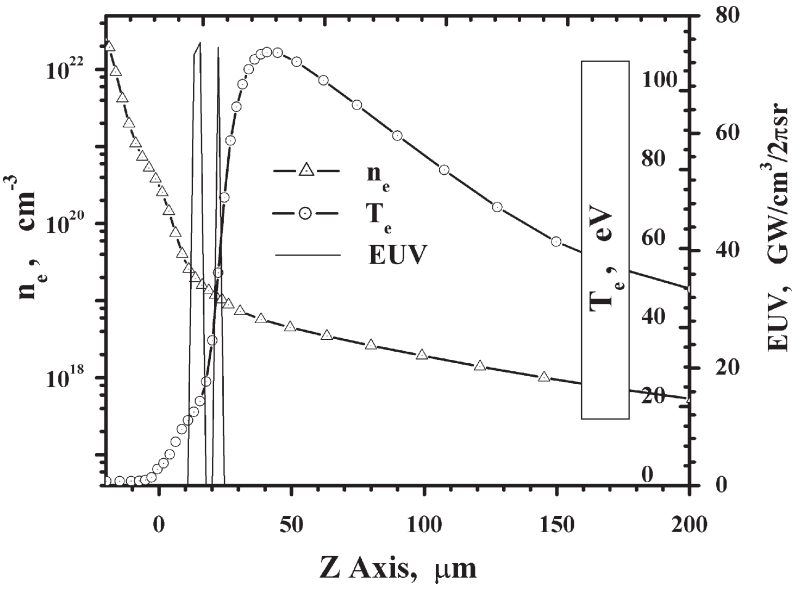

Figure 12. Electron concentration (n_e), electron temperature (T_e), and EUV capability of space along Z axis at $t = 9$ ns after irradiation start for planar Xe target.

time integration gives a wider EUV source form. Figure 12 plots the same parameters for the planar case, where EUV space capability is much smaller at the center of the laser spot.

CONCLUSIONS

We have presented an integrated model to describe the hydrodynamics and optical processes that occur in LPP devices. The model includes plasma motion processes, radiation transport, and EUV output, determined by the weight Monte Carlo method, laser light absorption, and thermal generation of the internal magnetic field. A two-temperature approximation was considered. Different sets of opacities for the MHD and EUV calculations were used: 3,693 spectral groups for Xe and 3,240 groups for Sn in a wide range, and near 2,500 spectral points for Xe and up to 5,000 spectral points for Sn within the EUV region. The developed models and numerical methods are being integrated into HEIGHTS, a computer simulation package developed by Argonne National Laboratory. Numerical simulations of the LPP device with droplet and planar targets showed very small dependence of the plasma parameters from the thermomagnetic source for laser-radiation power density up to 6.0×10^{11} W/cm^2. Correspondingly, the MHD code can be streamlined in the future for more efficient working by neglecting magnetic field and rank reduction of the operating matrixes. The HEIGHTS package, after reconstruction, will be a tool that can be used to study and optimize various LPP source parameters, such as EUV output, target design, and laser parameters.

REFERENCES

1. H. Meiling, V. Banine, P. Kürz, and N. Harned, Progress in the ASML EUV Program, *Proc. SPIE, Emerging Lithographic Technologies VIII*, Santa Clara, CA, vol. 5374, pp. 31–42, SPIE, Bellingham, WA, 2004.
2. U. Stamm, J. Kleinschmidt, K. Gäbel, H. Birner, I. Ahmad, D. Bolshukhin, J. Brudermann, T. Chinh, F. Flohrer, S. Götze, G. Hergenhan, D. Klöpfel, V. Korobotchko, B. Mader, R. Müller, J. Ringling, G. Schriever, and C. Ziener, EUV Source Power and Lifetime: The Most Critical Issues for EUV Lithography, *Proc. SPIE, Emerging Lithographic Technologies VIII*, Santa Clara, CA, vol. 5374, pp. 133–144, SPIE, Bellingham, WA, 2004.
3. A. Hassanein, V. Sizyuk, V. Tolkach, V. Morozov, and B. J. Rice, HEIGHTS Initial Simulation of Discharge-Produced Plasma Hydrodynamics and Radiation Transport for EUV Lithography, *Proc. SPIE, Emerging Lithographic Technologies VII*, Santa Clara, CA, vol. 5037, pp. 714–727, SPIE, Bellingham, WA, 2003.
4. A. Hassanein, V. Sizyuk, V. Tolkach, V. Morozov, and B. J. Rice, HEIGHTS Initial Simulation of Discharge Produced Plasma Hydrodynamics and Radiation Transport for Extreme Ultraviolet Lithography, *J. Microlithogr., Microfabr., Microsyst.*, vol. 3, pp. 130–138, 2004.
5. A. Hassanein, V. Sizyuk, V. Tolkach, V. Morozov, T. Sizyuk, B. J. Rice, and V. Bakshi, Simulation and Optimization of DPP Hydrodynamics and Radiation Transport for EUV Lithography Devices, *Proc. SPIE, Emerging Lithographic Technologies VIII*, Santa Clara, CA, vol. 5374, pp. 413–422, SPIE, Bellingham, WA, 2004.
6. Gábor Tóth and Dušan Odstrčil, Comparison of Some Flux Corrected Transport and Total Variation Diminishing Numerical Schemes for Hydrodynamic and Magnetohydrodynamic Problems, *J. Comput. Phys.,* vol. 128, pp. 82–100, 1996.
7. R. J. Leveque, *Finite Volume Methods for Hyperbolic Problems*, pp. 64–127, Cambridge University Press, Cambridge, UK, 2002.
8. R. Siegel and J. R. Howell, *Thermal Radiation Heat Transfer*, vol. III, Radiation Transfer with Absorbing, Emitting, and Scattering Media, chap. 6, NASA, Washington, DC, 1971.
9. K. C. Kannenberg and I. D. Boyd, Strategies for Efficient Particle Resolution in the Direct Simulation Monte Carlo Method, *J. Comput. Phys.,* vol. 157, pp. 727–745, 2000.
10. V. Tolkach, A. Hassanein, and V. Morozov, Development of Comprehensive Models for Opacities and Radiation Transport for IFE System, Argonne Natl. Lab. Rep. ANL-ET/02-23, Argonne, IL, 2002.
11. I. N. Burdonskii, V. V. Gavrilov, A. Yu. Gol'tsov, E. V. Zhuzhukalo, N. G. Koval'skii, V. N. Kondrashov, M. I. Pergament, B. N. Bazylev, G. S. Romanov, A. N. Smetannikov, V. I. Tolkach, M. O. Koshevoi, A. A. Rupasov, and A. S. Shikanov, Experimental, Numerical, and Theoretical Studies of X-Radiation and Radiative Thermal Conductivity in a Dense Laser Plasma with Multicharged Ions, *JETP*, vol. 79, pp. 879–890, 1994.
12. B. N. Bazylev, I. N. Burdonskii, V. V. Gavrilov, A. Yu. Gol'tsov, E. V. Zhuzhukalo, N. G. Koval'skii, V. N. Kondrashov, M. O. Koshevoi, M. I. Pergament, G. S. Romanov, A. A. Rupasov, A. S. Smetannikov, V. I. Tolkach, and A. S. Shikanov, Investigation of Energy Transfer in Plane Laser-Irradiated Targets with High X-Ray Conversion Efficiency, *Laser and Particle Beams*, vol. 12, pp. 355–359, 1994.
13. T. W. Johnston and J. M. Dawson, Correct Values for High-Frequency Power Absorption by Inverse Bremsstrahlung in Plasmas, *Phys. Fluids*, vol. 16, pp. 722–723, 1973.
14. M. V. Allmen and A. Blatter, Laser-Beam Interactions with Materials, in U. Gonser (ed.), *Springer Series in Material Science*, 2d ed., vol. 2, chap. 2, Springer-Verlag, Berlin, 1995.
15. L. Spitzer, *Physics of Fully-Ionized Gases*, 2d ed., pp. 136–143, Interscience, New York, 1962.

16. D. Düchs and H. R. Griem, Computer Study of the Dynamic Phase of a Small θ-Pinch, *Phys. Fluids*, vol. 9, pp. 1099–1109, 1966.
17. D. G. Colombant and N. K. Winsor, Thermal Force Term and Self-Generated Magnetic Fields in Laser-Produced Plasmas, *Phys. Rev. Lett.*, vol. 38, pp. 697–701, 1977.
18. C. E. Max, W. M. Manheimer, and J. J. Thompson, Enhanced Transport across Laser Generated Magnetic Fields, *Phys. Fluids*, vol. 21, pp. 128–139, 1978.
19. J. B. Chase, J. M. LeBlanc, and J. R. Wilson, Role of Spontaneous Magnetic Fields in a Laser-Created Plasma, *Phys. Fluids*, vol. 16, pp. 1142–1148, 1973.
20. V. Venkatakrishnan and D. J. Mavriplis, Implicit Solvers for Unstructured Meshes, *J. Comput. Phys.*, vol. 105, pp. 83–91, 1993.
21. P. J. Roach, *Computational Fluid Dynamics*, chap. 3.6, Hermosa, Albuquerque, NM, 1976.
22. O. V. Diyankov, I. V. Glazurin, and S. V. Koshelev, MAG—Two-Dimensional Resistive MHD Code using an Arbitrary Moving Coordinate System, *Comput. Phys. Commun.*, vol. 106, pp. 76–94, 1997.
23. G. Tóth, R. Keppens, and M. A. Botchev, Implicit and Semi-implicit Schemes in the Versatile Advection Code: Numerical Tests, *Astron. Astrophys.*, vol. 332, pp. 1159–1170, 1998.
24. A. A. Samarskii and Yu. P. Popov, *Difference Methods of the Gas Dynamics Problems Solution,* pp. 133–135, Nauka, Moscow, 1980 (in Russian).
25. S. Maxon and J. Eddleman, 2D MHD Calculations of the Plasma Focus, Lawrence Livermore Laboratory, Preprint 79067, pp. 10–11, 1977.
26. W. Wang, Q. L. Dong, and J. Zhang, Simulation Study of Conversion of Laser Energy into X-Rays in Laser Plasmas, *Phys. Plasmas,* vol. 9, pp. 3978–3983, 2002.
27. M. Fajardo, P. Zeitoun, and L.-C. Gauthier, Hydrodynamic Simulation of XUV Laser-Produced Plasmas, *Eur. Phys. J. D,* vol. 29, pp. 69–76, 2004.
28. K. Fujima, K. Nishihara, T. Kawamura, H. Furukawa, T. Kagawa, F. Koike, R. More, M. Murakami, T. Nishikawa, A. Sasaki, A. Sunahara, V. Zhakhovskii, T. Fujimoto, H. Tanuma, Theoretical Simulation of Extreme UV Radiation Source for Lithography, *Proc. SPIE, Emerging Lithographic Technologies VIII,* Santa Clara, CA, vol. 5374, pp. 405–412, SPIE, Bellingham, WA, 2004.